Enhancement of localized surface plasmon resonance detection by incorporating metal-dielectric double-layered subwavelength gratings

Seong Min Jang,[1] Donghyun Kim,[2] Seung Ho Choi,[3]
Kyung Min Byun,[4,*] and Sung June Kim[1,3]

[1]School of Electrical Engineering and Computer Science, Seoul National University, Seoul 151-742, South Korea

[2]School of Electrical and Electronic Engineering, Yonsei University, Seoul 120-749, South Korea

[3]Interdisciplinary Program of Bioengineering, Seoul National University, Seoul 152-742, South Korea

[4]Department of Biomedical Engineering, Kyung Hee University, Yongin 446-701, South Korea

*Corresponding author: kmbyun@khu.ac.kr

In this study, we investigated the enhanced sensing performance of a localized surface plasmon resonance (LSPR) biosensor by employing metal-dielectric double-layered subwavelength grating structures. The numerical results showed that the LSPR substrate with a dielectric spacer can provide not only a better sensitivity but also a significantly improved reflectance characteristic. While the presence of metallic gratings leads to a broad and shallow reflectance curve inevitably, the dielectric spacer can prevent the propagating surface plasmons from being interfered by the locally enhanced fields excited at the gold gratings, finally resulting in a strong and deep absorption band at resonance. Therefore, the proposed structure could potentially open a new possibility of the enhanced LSPR detection for monitoring biomolecular interactions of low molecular weights. © 2011 Optical Society of America

OCIS codes: 050.2770, 280.4788, 240.6680.

1. Introduction

Surface plasmon resonance (SPR) biosensors have gained widespread attention due to their analytical utility in the detection of biomolecular adsorption processes [1]. Since the pioneering works of Otto and Kretschmann [2,3], explorations into the use of SPR as a valuable tool for monitoring surface reactions have been intensive. Although the SPR technique has made significant advances by demonstrating its applications to waveguide, imaging, microscopy, and lithography formats [4–7], the vast majority of recent studies have been still focused on the characterization of a wide variety of layered biointeractions. In principle, one can measure tiny changes

in the refractive index caused by an immobilization of monolayer or multilayer quantities of biomaterials by tracking the shift of the resonance position [8].

Among a few parameters utilized in evaluating the performance quality of the SPR biosensor, the most important indicators are the sensitivity and the limit of detection (LOD). The numerical study by Piliarik and Homola defined the sensitivity as the ratio of the change in sensor output to the change in the quantity to be measured (e.g., the refractive index) and the LOD as the smallest change in the refractive index that produces a detectable change in the sensor output [9]. From the simple relation of LOD $= \sigma/S$, where σ is the standard deviation of noise of the sensor signal and S is the sensor sensitivity, it is obvious that the LOD characteristic can be improved by increasing the sensitivity S. In general, a traditional thin-film-based SPR biosensor can provide a

minimum LOD as high as 1×10^{-6} in a refractive index unit [10,11]. In practical sensing applications, however, it is often difficult to detect the target analytes of low molecular weights, due to various noise sources originating in optical systems and readout electronics as well as the light source [9].

Thus, in order to enhance both the sensitivity and the LOD, there have been numerous intriguing studies for amplifying the SPR signal. For example, some researchers proposed the strategies incorporating metallic nanoparticle-labeled target analytes [12]. Since metallic nanoparticles can offer an additional weight, this method was able to improve the resonance shift by more than an order, compared to the conventional SPR biosensor. However, its main drawback is that tagging biomolecules with colloidal metallic nanoparticles converts label-free SPR detection into a labeled one and is inevitably afflicted with troublesome target-specific labeling procedures. More recently, phase detection based on interferometry techniques was proposed to enhance the SPR sensor sensitivity [13–15]. Although the phase may produce more rapid changes than intensity, the phase signals have a small dynamic range and some limitations in the detection accuracy and the facilitation of a real-time measure. SPR detection in the IR region and optical fiber-based SPR biosensors with a Teflon layer were also explored for sensitivity enhancement [16,17].

Contrary to a few controversial investigations, our alternative SPR structure with metallic subwavelength gratings on a metal film, denoted as a single-layered grating-based localized SPR (SG-LSPR) structure, was intended to improve the sensitivity of the SPR biosensor significantly, while maintaining its intrinsic label-free detection [18,19]. In particular, our approach could serve as an effective way to increase a surface reaction area and to generate hot spots associated with a resonant excitation of localized surface plasmon (LSP) modes, resulting in a large sensitivity gain. Another important aspect is that the metallic gratings can be customized as desired to meet the specific sensitivity requirements.

On the other hand, despite the unique advantages concerning the sensitivity, the key issues about the LOD performance have not been addressed yet for our SG-LSPR substrates. It has been found from our previous studies that the use of metallic nanostructures deposited on a thin metal film makes the SPR curve broader and shallower [18,19]. It is attributable to a simultaneous excitation of SP and LSP modes, and, especially when the nanostructure size is increased, multiple LSP excitations and the damping of SP waves by destructive coupling with excited LSPs may occur [20]. These changes in the SPR characteristics resemble the dramatic variations in the SPR signal induced by colloidal gold nanoparticles [21]. It should be emphasized that the deformation of SPR curves can increase the uncertainty of the sensor output and affect its high standard error in

experimental measurement, finally producing a notable degradation of the LOD performance.

Therefore, the aim of our study is to achieve a well-designed SPR curve with a deep absorption band (i.e., a high signal-to-noise ratio) while maintaining the enhanced sensitivity by applying an intermediate dielectric spacer between the gold gratings and the underlying gold film. This study will serve as the first step to demonstrate the feasibility of the multilayered subwavelength grating structure for an enhanced SPR detection.

2. Numerical Model

For numerical analyses, we used rigorous coupled-wave analysis (RCWA) [22–24]. RCWA has been successful in explaining the experimental results of various nanosized periodic structures [25,26]. In this study, convergence of RCWA calculation was realized by including 30 space harmonic orders of the diffracted light. Also, using the finite-difference time-domain (FDTD) method, the distribution of near-field intensity on the sensor surface was visualized to estimate the field enhancement of LSP modes quantitatively. The minimum grid size for the FDTD was set to be 0.5 nm.

A schematic diagram of a double-layered grating-based (DG)-LSPR configuration with a dielectric spacer is shown in Fig. 1. One-dimensional arrays of infinitely long gratings with a gold and silicon dioxide (SiO_2) double layer are periodically patterned on a flat gold film. SiO_2 is chosen as a spacer material because it has been used as a representative dielectric in the fabrication processes. A 2-nm-thick chromium adhesion layer and a 40-nm-thick gold film are deposited on an SF10 prism substrate on which a polarized light at $\lambda = 633\,nm$ is incident. Binding analytes are modeled as a 1-nm-thick self-assembled monolayer (SAM). We assume 1,6-hexandiethiol for
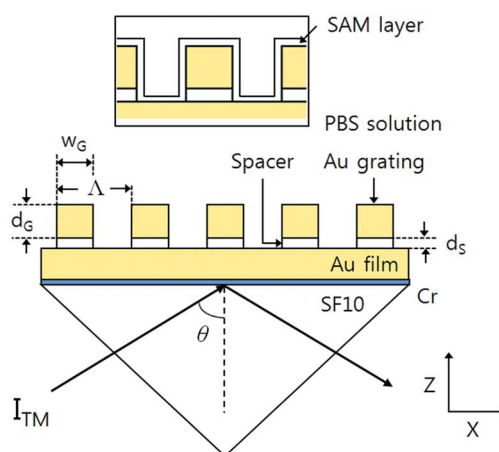

Fig. 1. (Color online) Schematic of a DG-LSPR substrate. TM-polarized light with $\lambda = 633\,nm$ propagating into an SF10 glass is incident through an attachment layer of chromium (2 nm), a thin gold film (40 nm), SiO_2 dielectric spacers (d_S), and gold gratings (d_G). Gold–SiO_2 grating structures of a rectangular profile have a width of w_G and a period of Λ. A 1-nm-thick SAM layer is assumed to cover the whole substrate surface uniformly.

the dielectric SAM that uniformly covers the whole sensor surface and approximate it as a homogeneous layer with a refractive index $n(\text{SAM}) = 1.52643$ [27]. The optical constants (n, k) of an SF10 glass substrate, chromium, gold, and SiO_2 are taken as (1.7231, 0), (3.48, 4.36), (0.18, 3.00), and (1.457, 0) at $\lambda = 633$ nm [28]. The refractive index of a phosphate-buffered saline (PBS) solution is assumed to be 1.33. The reflectance curve is obtained from RCWA calculations as the light incidence is scanned with an angular resolution of 0.01°. We consider the cross-sectional profile of a gold grating structure as a rectangle with a width of w_G and a depth of d_G, and thus a duty cycle equals w_G/Λ. The thickness of the dielectric spacer is denoted as d_S.

As a quantitative measure of the sensitivity improvement, we employed a sensitivity enhancement factor (SEF), which is the ratio of the SPR angle shift due to the SAM formation on an SG- or DG-LSPR substrate to that of a conventional SPR structure. While SPR curves are not shown for a conventional SPR system, the resonance angles with and without a SAM are 59.94° and 59.75° in PBS solution; thus, the reference resonance shift is 0.19°.

3. Results and Discussion

A. SEF Characteristics

The effect of duty cycle on the SPR characteristics is investigated for grating periods of $\Lambda = 50$ and 100 nm when the grating thickness is fixed at $d_G = 20$ nm. The periods of 50 and 100 nm were chosen based on our previous studies, demonstrating that an extremely sensitive LSPR structure typically requires metallic gratings of sub-50 nm linewidth, while the difficulty in an actual fabrication may increase [18,19]. Figure 2 shows that, for both periods, the SPR curves of an SG-LSPR biosensor can be significantly distorted depending on the duty cycle. Except for gratings at duty cycle = 0.1 and 0.9, determination of the resonance angle appears quite difficult. Although gold grating structures can provide a

Table 1. SEF Values of SG-LSPR Structures

	SEF	
Λ[nm]	Duty Cycle = 0.1	Duty Cycle = 0.9
50	10.42	4.58
100	4.89	—

notably enhanced sensitivity gain (see Table 1), the difficulties in an actual fabrication of extremely fine (i.e., duty cycle ~ 0.1) or densely packed (i.e., duty cycle ~ 0.9) gratings make the realization of a highly sensitive SG-LSPR substrate infeasible.

Figure 3 presents the SEF characteristics for DG-LSPR biosensors at $\Lambda = 50$ and 100 nm when the spacer thickness d_S increases from 0 to 110 nm. Note that the SEF values for SPR curves with a minimum reflectance at resonance >0.3 are not plotted because a shallow SPR dip is practically inappropriate for accurate detection of the binding events. For $\Lambda = 50$ nm, the DG-LSPR substrates provide a significant improvement of sensitivity at wide ranges of duty cycle and d_S, which implies performance reliability and robustness to fabrication errors in implementing the DG-LSPR substrates. The maximum SEF is obtained to be 14.1 at duty cycle = 0.1 and $d_S = 60$ nm, while the dielectric spacer with a duty cycle = 0.9 yields a gentle increment of SEF up to three times with its growing thickness.

In addition, when a duty cycle varies from 0.2 to 0.6, we can determine the optimal grating thickness for individual duty cycles. At this range, the SEF exhibits a rapid increase until the SEF reaches a maximum, which is primarily on account of an increasing surface reaction area, and then is decreased with an increasing d_S. This reduction of SEF is attributable to a confined penetration depth of SP waves. As an amplitude of the plasmon field decays exponentially when one moves away from the sensor surface, LSP excitations occurring at the gold grating become less efficient for very thick dielectric spacers. It is also interesting to find that the optimal spacer thickness with a peak
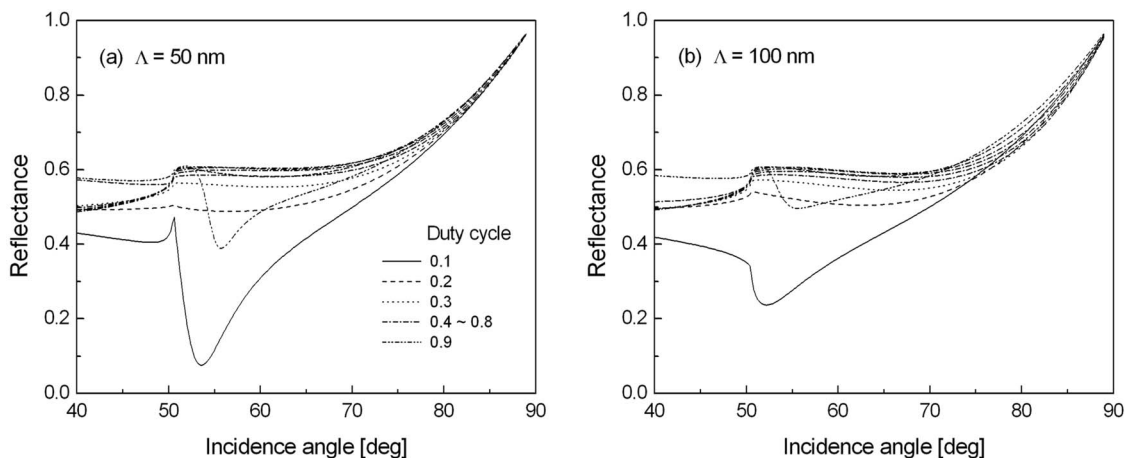

Fig. 2. SPR curves of an SG-LSPR substrate. Gold gratings have a period Λ of (a) 50 nm and (b) 100 nm when a duty cycle increases from 0.1 to 0.9 with a step of 0.1.
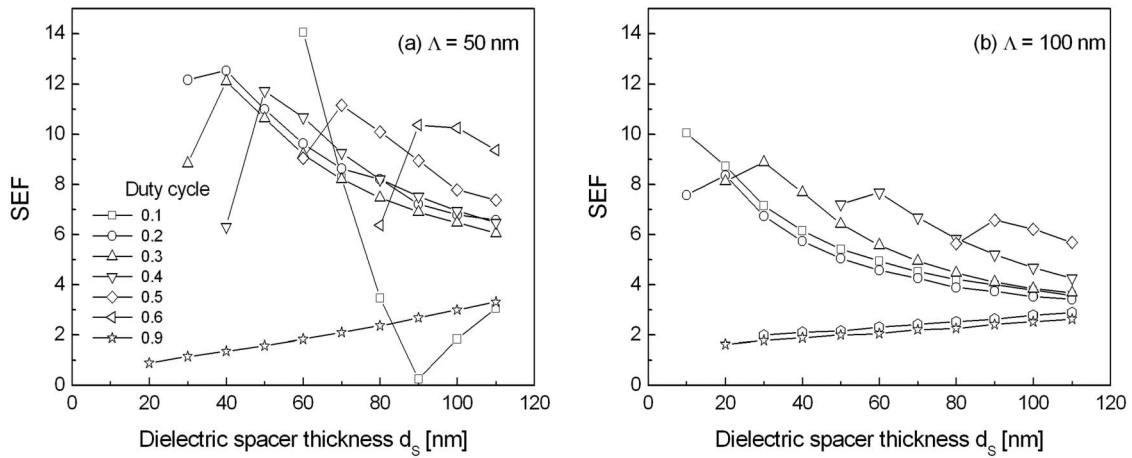
Fig. 3. SEF characteristics of a DG-LSPR substrate with respect to the duty cycle as a dielectric spacer thickness increases when Λ is (a) 50 nm and (b) 100 nm.

SEF grows when the duty cycle changes from 0.2 to 0.6. While its dependence on the duty cycle is little understood yet, an enhanced SEF at duty cycle > 0.6 could be possible for a dielectric spacer thicker than 110 nm. Figure 3(b) shows that the qualitative trends of the SEF at $\Lambda = 100$ nm resemble the case of $\Lambda = 50$ nm. The peak SEF is found to be 10.1 at duty cycle $= 0.1$ and $d_S = 10$ nm. While the numerical data for $\Lambda = 200$ nm are not shown here, its optimal grating structure with duty cycle $= 0.2$ and $d_S = 30$ nm yields a maximum SEF of 6.3. The growth of the peak SEF with a decrease of Λ is due to the fact that the overall surface reaction area increases when the grating period becomes smaller. Summarizing the results of Fig. 3, the subwavelength gold grating with a dielectric spacer leads to a notable improvement of sensitivity and the SEF characteristics are dependent on the duty cycle and the spacer thickness d_S as well as the period Λ.

B. Minimum Reflectance Characteristics

Figure 4 plots the minimum reflectance characteristics with respect to the spacer thickness. Because the

minimum reflectance at resonance is directly associated with the sensing contrast (i.e., the signal-to-noise ratio), smaller minimum reflectance values are required to accomplish a better LOD performance. For both grating periods, it is important to notice the remarkable reduction of minimum reflectance over the range of d_S. Since the propagating SP waves are less interfered by the LSP modes for a thick spacer, an effective excitation of resonant SPs may induce a strong absorption dip at the resonance. More interestingly, it is found that a substantial decrease of minimum reflectance is observed at larger d_S in accordance with an increase in duty cycle ranging from 0.2 to 0.6. This supports the assertion that the interference of LSP modes with SP waves occurs more strongly at a higher duty cycle and, thus, selecting a thick dielectric spacer would be suitable for wide gold gratings. From the results of Fig. 4, the reflectance characteristics can be significantly improved by inserting a dielectric spacer, which can prevent the excitation of SP waves from being coupled destructively and damped.
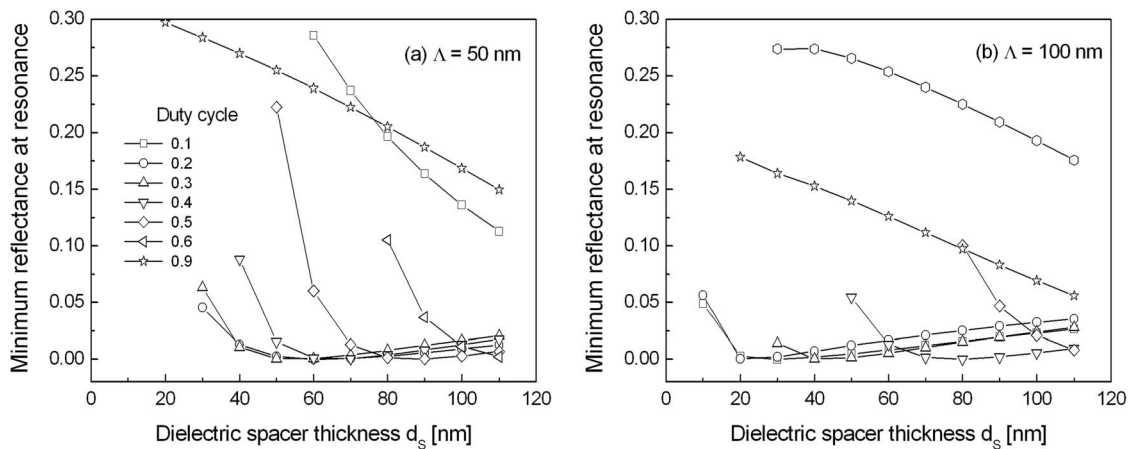

Fig. 4. Minimum reflectance characteristics of a DG-LSPR substrate with respect to the duty cycle as a dielectric spacer thickness increases when Λ is (a) 50 nm and (b) 100 nm.

Based on the quantitative metrics of SEF and minimum reflectance, optimal design parameters of the DG-LSPR substrate are determined to be a 20-nm-thick gold grating at $\Lambda = 50\,\text{nm}$ and duty cycle $= 0.2$ with a dielectric space of $d_S = 40\,\text{nm}$. This geometry results in a significantly enhanced sensitivity more than 12 times larger than that of a conventional SPR biosensor and a strong absorption band of minimum reflectance $= 0.01$.

C. Near-Field Characteristics

In order to verify the effect of a dielectric spacer, we visualize the enhanced plasmon fields near the sensor surface using the FDTD method. For comparison study, we have chosen subwavelength grating-based LSPR substrates with and without a 40-nm-thick spacer at $\Lambda = 50\,\text{nm}$ and duty cycle $= 0.2$. Figure 5(a) presents the field distribution E_Z of the SG-LSPR structure with $d_G = 20\,\text{nm}$ at the resonant incidence angle of $56.75°$. The FDTD calculation exhibits well-known features of LSP modes excited by metallic nanostructures. Locally enhanced fields, i.e., hot spots, are distributed at a very short distance from the surface in the vicinity of grating vertices [29]. Also, there are multiple peaks at each corner of the gold grating. Since the decay length of an LSP mode is shorter than the interpeak distance, the multiple peaks of each corner should be regarded as individual LSP modes. On the assumption that the electric field of an incident beam is of unit amplitude, maximum field amplitudes are obtained as $E_X = 30.2$, $H_Y = 3.5$, and $E_Z = 21.5$ for the SG-LSPR substrate. On the other hand, Fig. 5(b) presents that the maximum E_Z is notably enhanced. The peak localized field intensities of the DG-LSPR substrate with $d_S = 40\,\text{nm}$ are calculated as $E_X = 36.9$, $H_Y = 2.6$, and $E_Z = 47.1$ when an incidence beam has a resonance angle of $73.27°$.

As listed in Table 2, subwavelength gold gratings for various duty cycles at $\Lambda = 50$ and $100\,\text{nm}$ show an enhanced maximum field intensity of E_Z in the

Table 2. Maximum Intensity of E_Z Calculated for SG- and DG-LSPR Structures

	Max. of E_Z at $\Lambda = 50\,\text{nm}$	
Duty Cycle	SG-LSPR	DG-LSPR (d_S)
0.2	21.5	47.7 (40 nm)
0.3	17.8	47.7 (40 nm)
0.4	15.5	29.4 (50 nm)
0.5	12.7	27.0 (70 nm)
0.6	12.0	23.8 (90 nm)
	Max. of E_Z at $\Lambda = 100\,\text{nm}$	
VF	SG-LSPR	DG-LSPR (d_S)
0.2	34.0	67.3 (20 nm)
0.3	26.8	45.0 (30 nm)
0.4	21.5	42.7 (60 nm)
0.5	19.5	37.2 (90 nm)

presence of dielectric spacers compared to the results of the SG-LSPR structures. This poses an interesting postulation that the dielectric spacer plays a significant role in reducing a destructive interplay between LSP modes and propagating SP waves. Another important aspect is that, due to a strong overlap of the adsorbed target analytes with the excited LSP modes in the vicinity of gold grating vertices, biomolecular interactions occurring at the DG-LSPR substrate may contribute to a significant improvement of sensitivity more vigorously. In Fig. 6, the FDTD results exhibit resonant excitations of localized plasmons at the gold gratings as well as the coupling of incident waves to an SP and its propagation along the gold film in the same DG-LSPR structure as Fig. 5(b). The movie linked to Fig. 6 shows how the proposed LSPR substrate with a dielectric space produces both SP and LSP modes efficiently.

D. Effective Medium Analyses

The effective medium theory (EMT) is a theoretical model that interprets the optical properties of a composite medium based on the dielectric constants
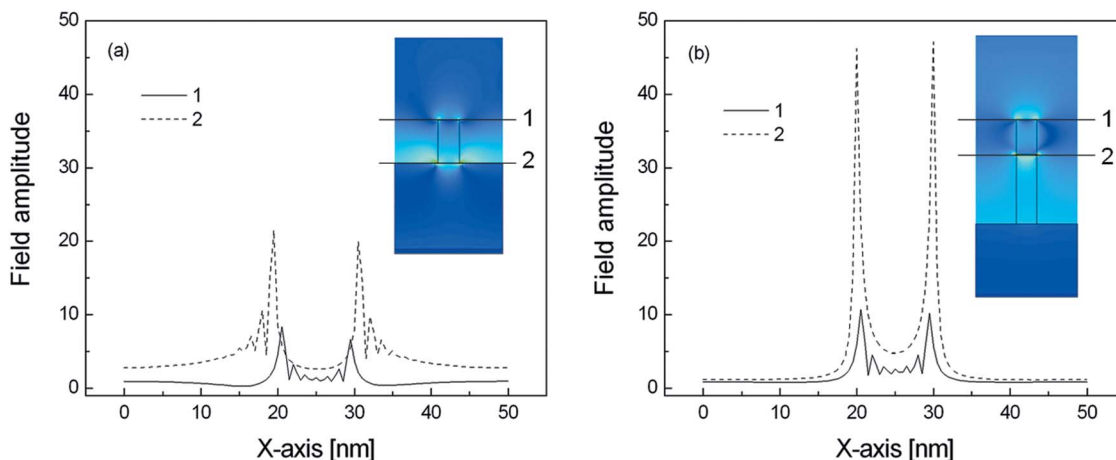

Fig. 5. (Color online) Horizontal field intensity distributions of E_Z for (a) SG-LSPR and (b) DG-LSPR structures with a gold grating of $\Lambda = 50\,\text{nm}$, duty cycle $= 0.2$, $d_G = 20\,\text{nm}$, and a dielectric spacer of $d_S = 40\,\text{nm}$. The insets are two-dimensional images obtained from the FDTD calculations normalized by the field intensity of 15.
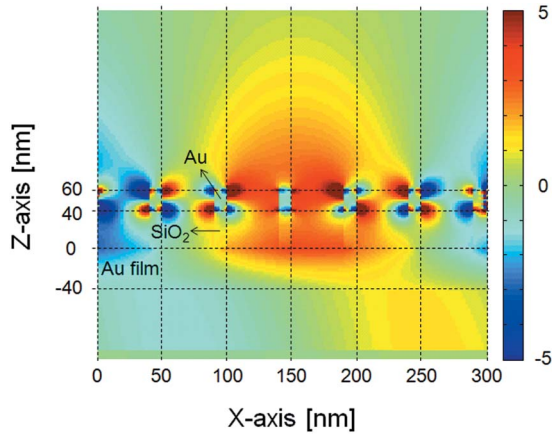
Fig. 6. (Color online) (Media 1) The field distribution of E_X for the optimal DG-LSPR structure shown in Fig. 5(b). The FDTD calculation results are normalized by a value of 5.

and the relative fractions of its components [30]. Since the use of an optically equivalent homogeneous layer for describing the far-field characteristics of an SG-LSPR structure was validated successfully in our earlier studies [31,32], we now intend to apply the effective medium for analyzing the reflectance characteristics of SG- and DG-LSPR substrates in the far field. The possibility of replacing fine gratings with a plamonically equivalent medium implies much facilitated implementation of an LSPR biosensor with a high signal-to-noise ratio. In particular, the EMT-based LSPR can be useful for complicated plasmonic substrates containing randomly distributed metallic nanostructures embedded in a host material [33–35], where the RCWA calculation cannot be employed.

When replacing the subwavelength metallic gratings with an equivalent homogeneous layer, exact determination of the effective permittivity has been known to be quite difficult because the EMT does not yield converged results and closed-form solutions do not exist for metallic gratings with a large and negative real part of permittivity. Recently, however, we demonstrated that the effective permittivity of a metallic nanostructure could be obtained by fitting to the RCWA results and the calculated effective medium showed a good agreement with RCWA in

the far field. In Fig. 7, the original DG-LSPR structure and its equivalent six-layer EMT model for calculating the reflectance characteristics are illustrated. $\varepsilon_{3,\text{eff}}$ and $\varepsilon_{4,\text{eff}}$ denote the effective permittivities of the SiO$_2$ spacer and the gold grating layer, respectively.

These effective permittivities can be obtained by simulating the DG-LSPR substrate with RCWA and subsequently fitting the exact results to a reflectance curve calculated by Fresnel coefficients for subwavelength grating structures. Then, we can replace the layer, including gold gratings, with a homogeneous effective layer. Using fitting-based effective permittivities, the reflectance is analytically described by computing the superposition of light waves reflected at each interface of two adjacent layers.

Analytical solution of the reflectance for TM-polarized light is represented in a 2×2 S matrix, which is a serial product of interface matrix I_{jk} and layer matrix L_j as follows [36]:

$$S = I_{01}L_1I_{12}L_2I_{23}L_3I_{34}L_4I_{45} = \begin{pmatrix} S_{11} & S_{12} \\ S_{21} & S_{22} \end{pmatrix}, \quad (1)$$

where j and k indicate the layer number. In Eq. (1), I_{jk} and L_j are expressed as

$$I_{jk} = \begin{pmatrix} 1 & r_{jk} \\ r_{jk} & 1 \end{pmatrix}, \quad (2)$$

$$L_j = \begin{pmatrix} e^{ik_{zj}d_j} & 0 \\ 0 & e^{-ik_{zj}d_j} \end{pmatrix}. \quad (3)$$

Here, r_{jk}, k_{zj}, and d_j represent the Fresnel reflection coefficient wave vector in the z direction, and the thickness of the jth layer, respectively. r_{jk} and k_{zj} are given by

$$r_{jk} = \frac{\left(\frac{k_{zj}}{\varepsilon_j} - \frac{k_{jk}}{\varepsilon_k}\right)}{\left(\frac{k_{zj}}{\varepsilon_j} + \frac{k_{jk}}{\varepsilon_k}\right)}, \quad (4)$$

$$k_{zj} = \sqrt{\varepsilon_j\left(\frac{\omega}{c}\right)^2 - k_x} \quad \text{with} \quad k_x = \sqrt{\varepsilon_0}\frac{\omega}{c}\sin\theta, \quad (5)$$
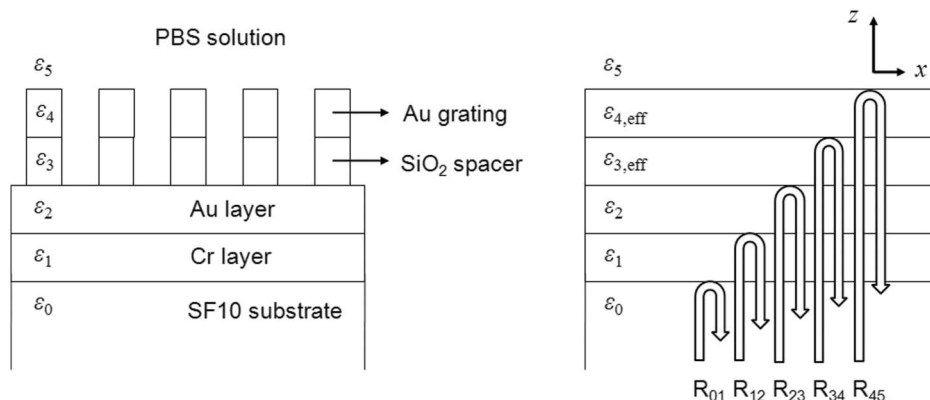

Fig. 7. Six-layer system of the DG-LSPR biosensor and its equivalent EMT model.

where ω is the angular frequency, c is the speed of light in free space, and θ is an incidence angle. Finally, reflectance R is obtained as

$$R = \left| \frac{S_{12}}{S_{22}} \right|^2. \qquad (6)$$

While the details are not drawn in Fig. 7, reflectance R_{jk} indicates a sum of the reflected lights at the interface I_{jk}, and it therefore involves individual lights with a multiple reflection inside the underlying layers.

Figure 8 shows the reflectance spectra calculated by RCWA and fitting-based EMT for gratings at $\Lambda = 100\,\mathrm{nm}$, duty cycle = 0.5, and $d_S = 90\,\mathrm{nm}$. By applying the fitting procedure to the reflectance characteristics of SG- and DG-LSPR structures, optical constants (n, k) of the homogeneous effective layers associated with the metallic grating and the dielectric spacer were determined to be (3.4468, 0.7805) and (1.4245, 0) at $\lambda = 633\,\mathrm{nm}$.

Since the total reflection intensities of $R_{\mathrm{SG_LSPR}}$ and $R_{\mathrm{DG_LSPR}}$ are expressed as a superposition of backward reflections at each interface between two adjacent layers, the minimum reflectance value can be obtained by summing up the individual reflected fields at the resonant incidence. First, for the SG-LSPR system with gold gratings of $\Lambda = 100\,\mathrm{nm}$ and duty cycle = 0.5, reflection field R_{45} is the most prominent, as shown in Fig. 9(a), while the other components are relatively insignificant. Thus, the amplitude of overall reflectance is as high as 0.752, which corresponds to the minimum reflectance of 0.566 in Fig. 9. Second, for a DG-LSPR structure with $d_S = 90\,\mathrm{nm}$, two reflection fields of R_{34} and R_{45} seem dominant. However, as the phase difference between R_{34} and R_{45} is almost 180°, destructive interference occurs and a deep SPR curve can be obtained (see Fig. 8). This result presents an interesting possibility that we may control or modulate the reflection intensity by engineering the geometry of a dielectric spacer.

Fig. 8. SPR curves of SG- and DG-LSPR structures calculated by RCWA (solid curve) and fitting-based EMT (dotted curve) when a period $\Lambda = 100\,\mathrm{nm}$, duty cycle = 0.5, and $d_S = 90\,\mathrm{nm}$.

E. Comparison Study of Sensor Performance

Finally, in regard to sensing applications of the DG-LSPR biosensor, it is important to show that the change in the resonance angle be highly sensitive and linearly proportional to a refractive index change at the sensor surface. Based on the assumption that the refractive index of the 1-nm-thick SAM layer (n_{SAM}) varies from 1.33, i.e., without a SAM in PBS solution, to 1.70 in accordance with the amount of adsorbed analytes, Fig. 10 shows the numerical results for conventional SPR structure and optimal LSPR profile with a subwavelength grating at $\Lambda = 50\,\mathrm{nm}$, $d_G = 20\,\mathrm{nm}$, duty cycle = 0.2, and $d_S = 40\,\mathrm{nm}$. For a conventional SPR system, the resonance angle shifts from 59.75° at $n_{\mathrm{SAM}} = 1.33$ to 60.07° at $n_{\mathrm{SAM}} = 1.70$, thus the net change is 0.32°. On the other hand, the SPR angle for optimal DG-LSPR structure is increased from 73.27° to 77.57°, implying about 13 times better sensitivity. In addition, based on the linear regression analysis, a linear relationship over a broad range of n_{SAM} is evident for both structures. The SPR change is extremely linear with $R = 0.9999$ for the conventional SPR substrate and $R = 0.9997$
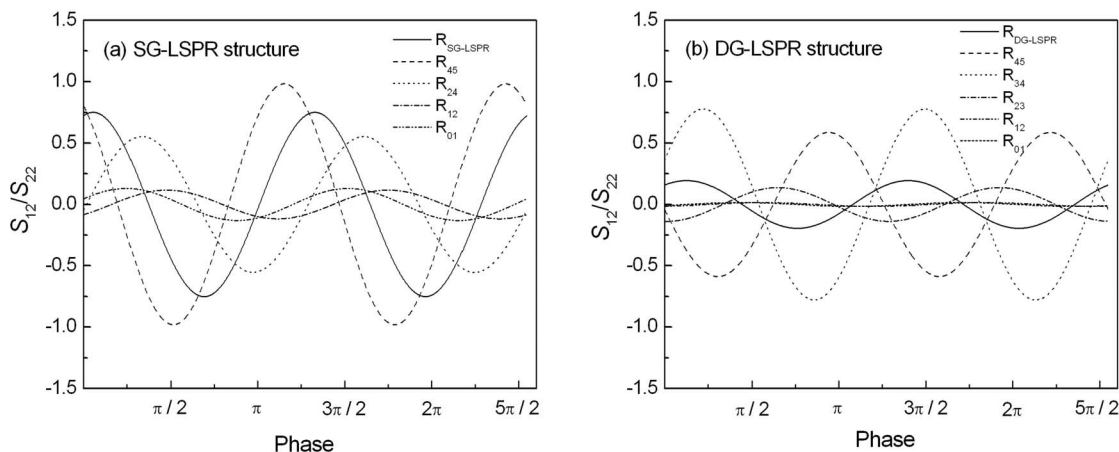

Fig. 9. Phase profiles of field elements reflected at each interface of (a) SG-LSPR and (b) DG-LSPR structures. The solid curves indicate the total reflectance.
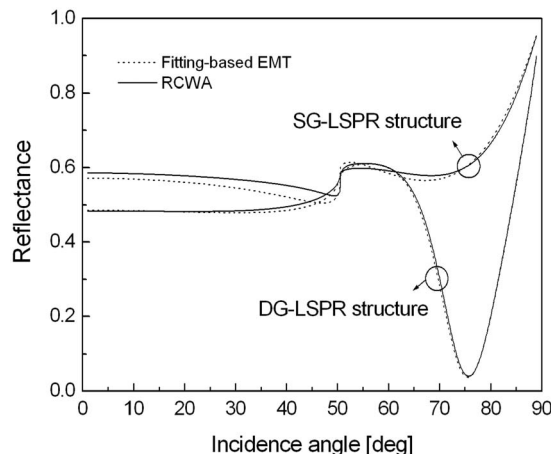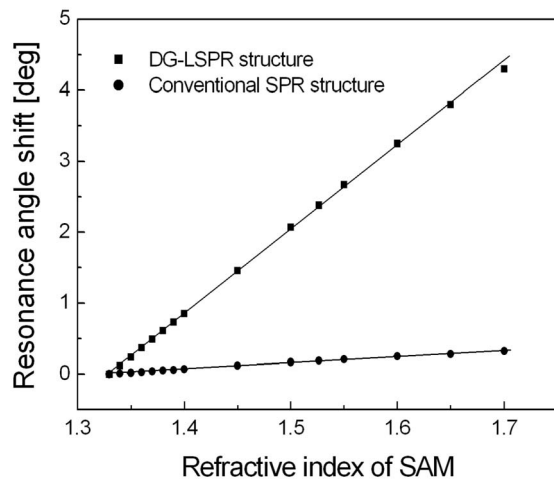
Fig. 10. Linear regression analyses between the resonance angle and the refractive index of a 1-nm-thick SAM in PBS solution for conventional gold substrate (circle) and optimal DG-LSPR substrate (square) with the highest SEF of 12.53 at $\Lambda = 50\,\text{nm}$, duty cycle = 0.2, $d_S = 40\,\text{nm}$, and $d_G = 20\,\text{nm}$. As the refractive index increases from 1.33 to 1.70, the SPR angle shifts with a high linearity in both cases, and, in particular, the sensitivity of the proposed DG-LSPR structure is 13 times greater than that of a conventional SPR substrate.

for the proposed DG-LSPR one, where the correlation coefficient R denotes the linearity obtainable in the sensor performance.

4. Conclusion

In summary, DG-LSPR biosensors with a dielectric spacer have been investigated to provide an enhanced sensitivity and a high quality of SPR signal. Compared with a conventional SPR structure and an SG-LSPR configuration, periodic gold–SiO_2 double-layered subwavelength gratings lead to a large amplification of the SPR shift for a wide range of duty cycle due to a strong excitation of LSP modes in gold gratings and an increased overall surface reaction area. Further, the SPR signal was significantly improved by the presence of a dielectric spacer, which is associated with the undamped SP waves. The impact of a dielectric spacer was also discussed by demonstrating the field distributions and the fitting-based EMT analyses.

The optimal DG-LSPR structure was determined as the grating at $\Lambda = 50\,\text{nm}$, duty cycle = 0.2, $d_G = 20\,\text{nm}$, and $d_S = 40\,\text{nm}$. For this LSPR substrate, the sensor performance presented a great SEF = 12.53, a strong and deep absorption band of minimum reflectance = 0.01, and a highly linear biosensing characteristic over a broad range of the refractive index. Considering rapid advances in fabrication techniques, such as e-beam or nanoimprint lithography, we envision that true realization of a DG-LSPR substrate and its applications to a sensitive detection for biomolecular reactions of low molecular weights will be readily feasible.

References

1. J. Homola, S. S. Yee, and G. Gauglitz, "Surface plasmon resonance sensors: review," Sens. Actuators B Chem. **54**, 3–15 (1999).
2. A. Otto, "Excitation of nonradiative surface plasma waves in silver by the method of frustrated total reflection," Z. Phys. **216**, 398–410 (1968).
3. E. Kretschmann, "Decay of nonradiative surface plasmons into light on rough silver films. Comparison of experimental and theoretical results," Opt. Commun. **6**, 185–187 (1972).
4. T. Srivastava, R. Das, and R. Jha, "Design considerations and propagation characteristics of channel Bragg-plasmon-coupled-waveguides," Appl. Phys. Lett. **97**, 213104 (2010).
5. H. J. Lee, T. T. Goodrich, and R. M. Corn, "SPR imaging measurement of 1D and 2D DNA micro-arrays created from microfluidic channels on gold thin films," Anal. Chem. **73**, 5525–5531 (2001).
6. B. Rothenhäusler and W. Knoll, "Surface-plasmon microscopy," Nature **332**, 615–617 (1988).
7. X. Guo, J. Du, Y. Guo, and J. Yao, "Large-area surface-plasmon polariton interference lithography," Opt. Lett. **31**, 2613–2615 (2006).
8. J. M. Pitarke, V. M. Silkin, E. V. Chulkov, and P. M. Echenique, "Theory of surface plasmons and surface-plasmon polaritons," Rep. Prog. Phys. **70**, 1–87 (2007).
9. M. Piliarik and J. Homola, "Surface plasmon resonance (SPR) sensors: approaching their limits?" Opt. Express **17**, 16505–16517 (2009).
10. L. S. Jung, C. T. Campbell, T. M. Chinowsky, M. N. Mar, and S. S. Yee, "Quantitative interpretation of the response of surface plasmon resonance sensors to adsorbed films," Langmuir **14**, 5636–5648 (1998).
11. X. D. Hoa, A. G. Kirk, and M. Tabrizian, "Towards integrated and sensitive surface plasmon resonance biosensors: a review of recent progress," Biosens. Bioelectron. **23**, 151–160 (2007).
12. L. He, M. D. Musick, S. R. Nicewarner, F. G. Salinas, S. J. Benkovic, M. J. Natan, and C. D. Keating, "Colloidal Au-enhanced surface plasmon resonance for ultrasensitive detection of DNA hybridization," J. Am. Chem. Soc. **122**, 9071–9077 (2000).
13. C. M. Wu, Z. C. Jian, S. F. Joe, and L. B. Chang, "High-sensitivity sensor based on surface plasmon resonance and heterodyne interferometry," Sens. Actuators B Chem. **92**, 133–136 (2003).
14. A. V. Kabashin and P. I. Nikitin, "Interferometer based on a surface-plasmon resonance for sensor applications," Quantum Electron. **27**, 653–654 (1997).
15. A. V. Kabashin and P. I. Nikitin, "Surface plasmon resonance interferometer for bio- and chemical-sensors," Opt. Commun. **150**, 5–8 (1998).
16. R. Jha and A. K. Sharma, "High-performance sensor based on surface plasmon resonance with chalcogenide prism and

aluminum for detection in infrared," Opt. Lett. **34**, 749–751 (2009).

17. R. Jha, R. K. Verma, and B. D. Gupta, "Surface plasmon resonance-based tapered fiber optic sensor: sensitivity enhancement by introducing a Teflon layer between core and metal layer," Plasmonics **3**, 151–156 (2008).

18. K. M. Byun, S. J. Kim, and D. Kim, "Design study of highly sensitive nanowire-enhanced surface plasmon resonance biosensors using rigorous coupled wave analysis," Opt. Express **13**, 3737–3742 (2005).

19. K. Kim, D. J. Kim, S. Moon, D. Kim, and K. M. Byun, "Localized surface plasmon resonance detection of layered biointeractions on metallic subwavelength nanogratings," Nanotechnology **20**, 315501 (2009).

20. I. Pockrand, "Surface plasma oscillations at silver surfaces with thin transparent and absorbing coatings," Surf. Sci. **72**, 577–588 (1978).

21. L. A. Lyon, M. D. Musick, and M. J. Natan, "Colloidal Au-enhanced surface plasmon resonance immunosensing," Anal. Chem. **70**, 5177–5183 (1998).

22. M. G. Moharam and T. K. Gaylord, "Rigorous coupled-wave analysis of metallic surface-relief gratings," J. Opt. Soc. Am. A **3**, 1780–1787 (1986).

23. L. Li, "Multilayer modal method for diffraction gratings of arbitrary profile, depth, and permittivity," J. Opt. Soc. Am. A **10**, 2581–2591 (1993).

24. L. Li and C. W. Haggans, "Convergence of the coupled-wave method for metallic lamellar diffraction gratings," J. Opt. Soc. Am. A **10**, 1184–1189 (1993).

25. Y. Kanamori, K. Hane, H. Sai, and H. Yugami, "100 nm period silicon antireflection structures fabricated using a porous alumina membrane mask," Appl. Phys. Lett. **78**, 142–143 (2001).

26. S. Park, G. Lee, S. H. Song, C. H. Oh, and P. S. Kim, "Resonant coupling of surface plasmons to radiation modes by use of dielectric gratings," Opt. Lett. **28**, 1870–1872 (2003).

27. E. Hutter, S. Cha, J. F. Liu, J. Park, J. Yi, J. H. Fendler, and D. Roy, "Role of substrate metal in gold nanoparticle enhanced surface plasmon resonance imaging," J. Phys. Chem. B **105**, 8–12 (2001).

28. E. D. Palik, *Handbook of Optical Constants of Solids* (Academic, 1985).

29. L. Qin, S. Zou, C. Xue, A. Atkinson, G. C. Schatz, and C. A. Mirkin, "Designing, fabricating, and imaging Raman hot spots," Proc. Natl. Acad. Sci. USA **103**, 13300–13303 (2006).

30. S. M. Rytov, "Electromagnetic properties of a finely stratified medium," Sov. Phys. JETP **2**, 466–475 (1956).

31. S. Moon and D. Kim, "Fitting-based determination of an effective medium of a metallic periodic structure and application to photonic crystals," J. Opt. Soc. Am. A **23**, 199–207 (2006).

32. D. Kim and S. J. Yoon, "Effective medium based analysis of nanowire-mediated localized surface plasmon resonance," Appl. Opt. **46**, 872–880 (2007).

33. J. Fu, B. Park, and Y. Zhao, "Nanorod-mediated surface plasmon resonance sensor based on effective medium theory," Appl. Opt. **48**, 4637–4649 (2009).

34. D. Dalacu and L. Martinu, "Spectroellipsometric characterization of plasma-deposited Au/SiO$_2$ nanocomposite films," J. Appl. Phys. **87**, 228–235 (2000).

35. S.-J. Chen, F. C. Chien, G. Y. Lin, and K. C. Lee, "Enhancement of the resolution of surface plasmon resonance biosensors by control of the size and distribution of nanoparticles," Opt. Lett. **29**, 1390–1392 (2004).

36. S. H. Choi and K. M. Byun, "Investigation on an application of silver substrates for sensitive surface plasmon resonance imaging detection," J. Opt. Soc. Am. A **27**, 2229–2236 (2010).